JOURNAL OF AIRCRAFT
Vol. 45, No. 3, May–June 2008

Unsteady Simulations of Bell-Agusta 609 Rotor Undergoing Higher Harmonic Oscillation

Chunhua Sheng*
Mississippi State University, Starkville, Mississippi 39759
and
Jim C. Narramore†
Bell Helicopter Textron, Inc., Fort Worth, Texas 76101

DOI: 10.2514/1.32877

The unsteady flowfield of a Bell-Agusta 609 rotor is numerically investigated with an unsteady Reynolds-averaged Navier–Stokes flow solver based on unstructured grid topology. The geometry considered is a three-bladed rotor that is undergoing a higher harmonic blade-pitch oscillation. Methodology is presented to model the multiblade cyclic motion that is superimposed on the basic motion. The unsteady airloads and blade-vortex interaction phenomenon are investigated for hovering and forward flight conditions. Numerical simulations indicate a significant impact of the blade-pitch oscillation on the tip-vortex structure and associated blade-vortex interaction.

Nomenclature

C	=	blade chord, ft
C_d	=	drag coefficient
C_l	=	lift coefficient
C_m	=	hub moment coefficient
C_p	=	pressure coefficient
f_r	=	cyclic pitch rate, Hz
M_{tip}	=	hover tip Mach number
M_∞	=	freestream Mach number
M^2c_m	=	sectional pitching moment
M^2c_n	=	sectional normal force
t	=	physical time, s
α	=	angle of attack, deg
α_1	=	alternating angle of attack, deg
β_0	=	coning angle, deg
β_{1c}	=	longitudinal cyclic pitch angle, deg
β_{1s}	=	lateral cyclic pitch angle, deg
$\beta(t)$	=	flap angle, deg
δ	=	descending angle, deg
θ_0	=	collective pitch angle, deg
θ_{1c}	=	longitudinal tip-path-plane tilt angle, deg
θ_{1s}	=	lateral tip-path-plane tilt angle, deg
$\theta(t)$	=	pitch angle, deg
μ	=	advance ratio, M_∞/M_{tip}
ϕ	=	phase angle, deg
$\psi(t)$	=	azimuth angle, deg
Ω	=	rotor rotational speed, 1/s

I. Introduction

THE flowfield of a rotorcraft is highly unsteady and three dimensional. This complexity is attributed to the unique aerodynamic features that a rotary wing exhibits and inherently coupled nature of interactive disciplines among aerodynamics, stability and control, aeroelastics, and acoustics. Successful aerodynamic analysis of this problem requires accurate capability and enabling technology for modeling unsteady, three-dimensional flowfields, transonic flow with shocks, reversed flow, dynamic stall, vortical flows, rigid body motions, and structural deformation. Currently, there are new concepts under development to improve rotorcraft aerodynamic and dynamic characteristics, as well as for noise, vibration, and load alleviation. One particular application is called higher harmonic control (HHC) [1,2] that applies high-frequency cyclic inputs to the rotor blades, resulting in 2, 3, and 4-per-revolution blade-pitch oscillations. There were evidences that a large reduction of blade-vortex interaction (BVI) noise was achieved on a XV-15 rotor model test conducted at NASA Ames Research Center [3]. These methods, however, require extensive mapping of the combinations of conditions to achieve significant noise reduction, and often coincide with increases in vibration level on the rotor. To better understand the complex aerodynamic effect and underlying mechanism of the rotor higher harmonic oscillation on noise, vibration, and load alleviation, advanced computational capabilities are required to capture the complexity of active rotor response and flow physics. Improved understanding of the unsteady flow phenomenon associated with the higher harmonic cyclic blade motion helps guide future development of these concepts for better aerodynamic, structural, and acoustic performances.

Over the last two decades, computational fluid dynamics (CFD) methods have evolved from early transonic small-disturbance theory [4] to the current Euler and Navier–Stokes simulations [5,6], and have become useful rotor analysis and design tools due to advancement of modern high performance computer architectures. A recent trend is to couple the rotor CFD codes with structural and/or acoustic analysis [7,8] to account for aerodynamic, structural, and acoustic interactions. Although most of the rotor CFD analyses are based on the structured overset grid topology [5,6,9] to alleviate the difficulty for dynamic rotor blade motion, intensive gridding efforts are necessary to handle realistic and complicated rotor geometries, grid refinement/adaptation, and multidisciplinary coupling. On the other hand, unstructured grid rotor CFD methods [10,11] provide unique advantages compared to the structured grid counterpartners, which will be used in the present investigation.

The objective of this study is to present an unstructured grid CFD method [11,12] to investigate the unsteady flowfield of a Bell-Agusta 609 rotor undergoing higher harmonic blade-pitch oscillation. An embedded dynamic moving grid methodology is used to account for the actual blade pitching and flapping motions and to preserve the higher-order numerical accuracy. A unique feature of the current method is that it allows for multiple relative blade motions involving different control schemes, and does not require any interpolation to

Presented as Paper 3928 at the 25th AIAA Applied Aerodynamics Conference, Miami, FL, 25–28 June 2007; received 20 June 2007; revision received 16 August 2007; accepted for publication 19 August 2007.

*Associate Research Professor of Computational Engineering, Computational Simulation and Design Center. Senior Member AIAA.
†Chief of Aerodynamics.

exchange data across the moving interfaces. Two typical rotor operating conditions, the hover and forward-descent flights, are investigated to assess the effects of the higher harmonic cyclic blade pitch on aerodynamic performance, unsteady loadings, and blade-vortex interaction phenomenon. The simulation results of the present study may provide insights for the understanding of the complex physics associated with the higher harmonic blade-pitch oscillation for the future improvement of rotorcraft performance.

II. Mathematic Formulation

A. Governing Equations

The three-dimensional unsteady Reynolds-averaged Navier–Stokes equations are cast in a finite-volume form with the primitive variables $\boldsymbol{q}$. It represents a system of conservation laws for a control volume that relates the rate of change of a vector of average state variables to the flux through the control surface. A global preconditioning technique [13] is introduced into the compressible governing equations to compute both low- and high-speed rotor flows. The conservative form of the governing equations, after introducing a preconditioning matrix Γ_q^{-1}, can be written as

$$M\Gamma_q^{-1}\frac{\partial}{\partial t}\int_\Omega \boldsymbol{q}\,\mathrm{d}V + \oint_{\partial\Omega}\boldsymbol{F}\cdot\hat{\boldsymbol{n}}\,\mathrm{d}A = 0 \tag{1}$$

where Γ_q^{-1} is a constant diagonal matrix that only depends on the reference Mach number M_r,

$$\Gamma_q^{-1} = \mathrm{diag}[1,\ \ 1,\ \ 1,\ \ 1,\ \ 1/\beta(M_r)] \tag{2}$$

and M is the transformation matrix from conservative variables $\boldsymbol{Q} = (\rho, \rho u, \rho v, \rho w, \rho e_t)$ to primitive variables $\boldsymbol{q} = (\rho, u, v, w, p)$. $\boldsymbol{F}$ is the vector of the flux on the face of the control volume, which can be written in the normal direction as

$$\boldsymbol{F}\cdot\hat{\boldsymbol{n}} = \begin{bmatrix} \rho\Theta \\ \rho u\Theta + n_x p - T_x \\ \rho v\Theta + n_y p - T_y \\ \rho w\Theta + n_z p - T_z \\ \rho h_t\Theta - n_t E_c p - (\gamma-1)M_r^2(uT_x + vT_y + wT_z) + Q_n \end{bmatrix} \tag{3}$$

where Θ is the normal velocity on the control surface, $E_c = (\gamma - 1)M_r^2$ is an Eckert number, and T_x, T_y, and T_z are the viscous flux components

$$\begin{aligned} T_x &= n_x\tau_{xx} + n_y\tau_{xy} + n_z\tau_{xz} \\ T_y &= n_x\tau_{yx} + n_y\tau_{yy} + n_z\tau_{yz} \\ T_z &= n_x\tau_{zx} + n_y\tau_{zy} + n_z\tau_{zz} \end{aligned}$$

$$\begin{aligned} \tau_{xx} &= \frac{\mu}{Re}\frac{2}{3}\left(2\frac{\partial u}{\partial x} - \frac{\partial v}{\partial y} - \frac{\partial w}{\partial z}\right) & \tau_{xy} &= \tau_{yx} = \frac{\mu}{Re}\left(\frac{\partial u}{\partial y} + \frac{\partial v}{\partial x}\right) \\ \tau_{yy} &= \frac{\mu}{Re}\frac{2}{3}\left(2\frac{\partial v}{\partial y} - \frac{\partial u}{\partial x} - \frac{\partial w}{\partial z}\right) & \tau_{xz} &= \tau_{zx} = \frac{\mu}{Re}\left(\frac{\partial u}{\partial z} + \frac{\partial w}{\partial x}\right) \\ \tau_{zz} &= \frac{\mu}{Re}\frac{2}{3}\left(2\frac{\partial w}{\partial z} - \frac{\partial u}{\partial x} - \frac{\partial v}{\partial y}\right) & \tau_{yz} &= \tau_{zy} = \frac{\mu}{Re}\left(\frac{\partial v}{\partial z} + \frac{\partial w}{\partial y}\right) \end{aligned} \tag{4}$$

The heat fluxes are

$$\begin{aligned} Q_n &= n_x q_x + n_y q_y + n_z q_z & q_x &= -\frac{1}{Re}\frac{\mu}{P_r}\frac{\partial T}{\partial x} \\ q_y &= -\frac{1}{Re}\frac{\mu}{P_r}\frac{\partial T}{\partial y} & q_z &= -\frac{1}{Re}\frac{\mu}{P_r}\frac{\partial T}{\partial z} \end{aligned} \tag{5}$$

Note that the above equations are normalized by the following reference values: density ρ_r, velocity U_r, temperature T_r, pressure $\rho_r U_r^2$, length L_r, time L_r/U_r, energy and enthalpy $C_p T_r$, and viscosity μ_r. The Reynolds number is defined as $Re = \rho_r U_r L_r/\mu_r$, and the Prandtl number as $P_r = \mu C_p/k$. Detailed descriptions of the preconditioned equations for the arbitrary Mach number solution algorithm can be found in [14,15].

B. Time Advancement Scheme

The above governing equation (1) is discretized by a node-based finite-volume implicit scheme, which can be written as

$$M\Gamma_q^{-1}\frac{\boldsymbol{q}_0^{n+1} - \boldsymbol{q}_0^n}{\Delta t}\Delta V + \sum_{j=1}^{JM}\boldsymbol{F}_j^{n+1}\Delta\boldsymbol{A}_j = 0 \tag{6}$$

where Δt is the time increment between step n and $n+1$. Subscript 0 denotes the indices of the central node of the control volume, and j denotes the dual faces ($j = 1, 2, \ldots, JM$) that make up the control surface. ΔV and ΔA are the finite volume and the area of the dual faces for the given control volume. Newton's method is introduced to solve the above nonlinear system of Eq. (6). Denote the unsteady residual on the left-hand side of Eq. (6) as

$$N(\boldsymbol{q}_0^{n+1}) = M\Gamma_q^{-1}\frac{\boldsymbol{q}_0^{n+1} - \boldsymbol{q}_0^n}{\Delta t}\Delta V + \sum_{j=1}^{JM}\boldsymbol{F}_j^{n+1}\Delta\boldsymbol{A}_j = 0 \tag{7}$$

Newton's method would be to solve the following equation:

$$N'(\boldsymbol{q}_0^{n+1,m})(\boldsymbol{q}_0^{n+1,m+1} - \boldsymbol{q}_0^{n+1,m}) = -N(\boldsymbol{q}_0^{n+1,m}) \tag{8}$$

where N' is the system Jacobian matrix, including both inviscid and viscous flux Jacobian matrices, and a diagonal matrix from the time derivative term in Eq. (6). The numerical flux $\boldsymbol{F}$ on the face of a control volume is computed with a second-order Roe flux approximation based on a preconditioned eigensystem [14,15]. The above Newton's method results in a linear system of equations, which can be solved with symmetric Gauss–Seidel relaxations to obtain an approximate solution at each Newton step m. For unsteady flow calculations, a series of Newton subiterations (normally four) are required to ensure the temporal accuracy for a time-dependent solution marching from time step n to $n+1$, where eight symmetric Gauss–Seidel relaxations are sufficient to converge the solution to the satisfying level.

C. Embedded Dynamic Moving Grid

A model for the rigid blade flapping and pitching motion is used in this study. Because Eulerian angles are a convenient way of expressing the motion of rotating bodies in an inertial frame, the periodic blade pitch and flapping motions can be approximated by a Fourier series as follows, which is truncated to the first harmonic corresponding to the blade motion [16]:

$$\begin{aligned} \beta(t) &= \beta_0 + \beta_{1c}\cos(2\pi f_r t + \phi) + \beta_{1s}\sin(2\pi f_r t + \phi) \\ \theta(t) &= \theta_0 + \theta_{1c}\cos(2\pi f_r t + \phi) + \theta_{1s}\sin(2\pi f_r t + \phi) \\ \psi(t) &= \Omega\cdot t \end{aligned} \tag{9}$$

In the present study, the complex rotor blade motion such as higher harmonic blade oscillation is modeled using an embedded dynamic moving grid technique, called nested parent and child volumes as illustrated in Fig. 1. In this approach, the motion of the blade within a volume is considered as a combination of its own motion and that of its parent with different control parameters, as defined in Eq. (9). Because there is no limitation on the number of parent and child volumes for a computational mesh, meaning that a child volume may have its own child or a parent volume may have its own parent, this provides a flexible way to control the rotor blade position with complex moving schemes. The current methodology is very suitable for modeling the helicopter rotor with trim, active blade-pitch control, multiple rotors, as well as rotor-airframe interactions in a complete rotorcraft configuration [17]. Figure 1 shows the Bell-Agusta 609 rotor computational model that contains a parent volume

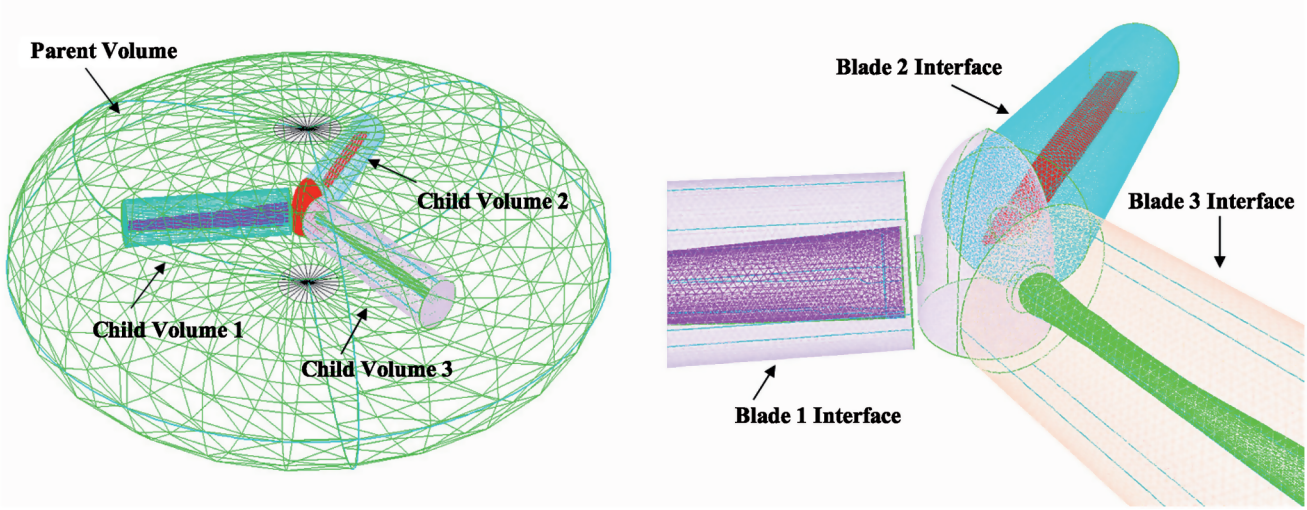

Fig. 1 Geometric model with parent and child volumes for Bell-Agusta 609 rotor (left: overview, right: rotor hub clearance).

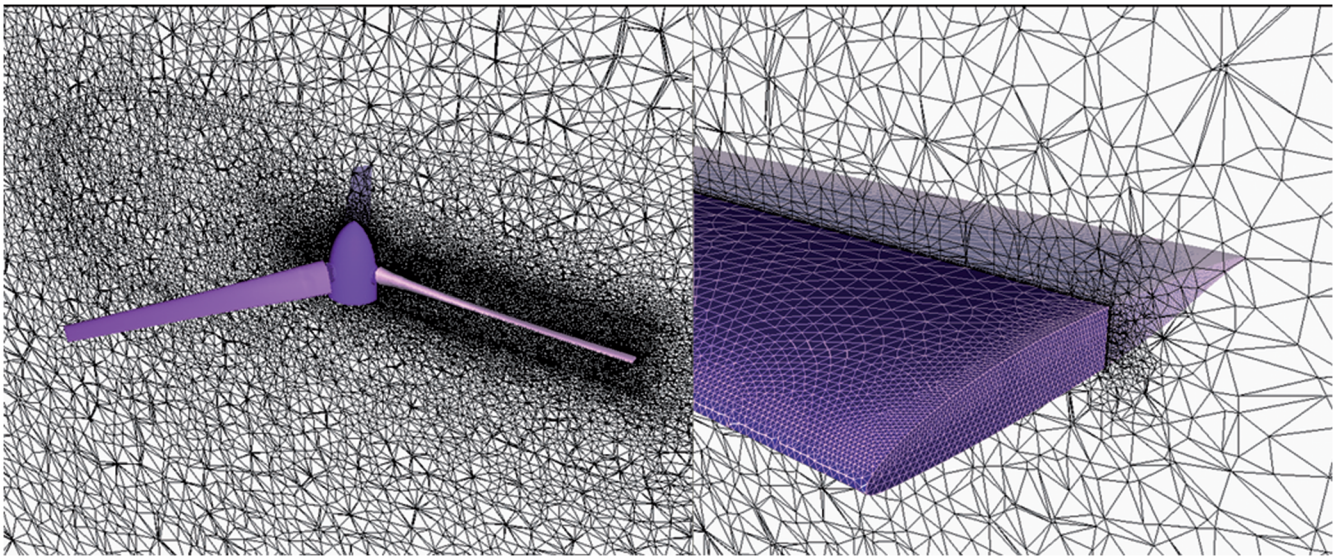

Fig. 2 Unstructured surface and volume meshes for Bell-Agusta 609 rotor (left: overview, right: rotor tip).

and three child volumes. The parent volume only has basic rotating motion, while three child volumes involve cyclic motion. The parent volume has its own parent (not shown in the figure) which is stationary and connects to the far-field boundary.

The embedded dynamic moving grid approach involves unstructured grid generation and reconnection before and during the solution process. This consists of predefining one or more moving interfaces for each parent and child volume when generating the computational mesh. Attention must be paid to the location of the relative moving interface, which should be located within the isotropic grid region and away from the boundary layers. This may impose certain restrictions on the boundary layer growth off the solid wall, especially in the region that has very small clearance gap between the rotor tip and airframe or hub. A rule of thumb is that the point spacing on the solid surface cannot be more than half of the clearance distance with the current anisotropic volume grid generator [18]. Following this rule will ensure that the boundary layer growth is constrained so that the interface is located in the isotropic grid region, even in the small clearance region. During the solution process, there is a relative motion between the parent and child volumes. An isotropic inviscid grid generator routine [18] is called from the solver to reconnect cells on one side of the moving interface. Because the reconnection of cells only works in the isotropic grid region, this requires that at least two layers of the isotropic grid cells on each side of the interface are needed to properly connect cells to the interface. The unstructured grid generator is integrated into the flow solver to provide smooth and robust grid reconnection as the rotor blade changes its position in a time marching solution. A very unique advantage of the present method over the overset grid approach is that no interpolation is required on the interface to exchange information between two relative moving grids, because all the nodes are fully connected in the entire domain during the solution process for the current node-based finite-volume scheme. This is especially beneficial to the higher-order numerical schemes where the same numerical accuracy is preserved on the interface as in the interior domain. It also helps reduce the numerical dissipation of the vortical flow in the field and guarantees the continuity of solutions across the interface. In terms of the overhead of the CPU time associated with reconnecting cells in the solution process, it was found that the extra cost is about 10–15% on most unsteady flow simulations.

III. Results and Discussion

The configuration considered in the current study is a three-bladed Bell-Agusta 609 rotor, which is a similar configuration to an XV-15 rotor. The blade is highly twisted and has a radius of 13 ft. The design rotor speed is 569 rpm, resulting in a tip speed of 775.0 ft/s or tip Mach number of 0.69. The Reynolds number is 99×10^6 based on the diameter of the blade and the tip velocity. Two flow conditions

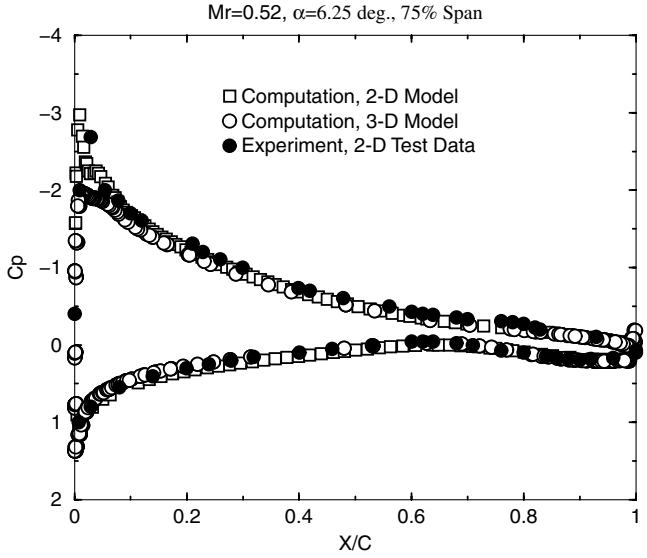

Fig. 3 Validation of Bell-Agusta 609 rotor computations and 2-D test data at 75% blade span.

were considered in this study, including a hover and a forward-descend flight. A higher-frequency blade-pitch oscillation is introduced in each blade, resulting in a pitch rate of 4 cycles per rotor revolution. The purpose of this study is to investigate the influence of the blade-pitch oscillation on the unsteady airloads, the vortical flowfield, and the blade-vortex interaction phenomenon for the Bell-Agusta 609 rotor. The unsteady pressure-field distributions obtained from this study may be used as input for a separate acoustic analysis.

The computational mesh for the Bell-Agusta 609 rotor was generated with an unstructured grid generation tool [18]. To accommodate the rotor blade cyclic motion, a total of four volume grids were generated including a stationary outer volume grid, a rotating parent volume enclosing the entire rotor, and three child volumes enclosing each blade. These volume grids were merged together to form a single computational domain, but with different volume tags for defining grid movement purpose. The computational mesh has 2.29×10^6 nodes and 7.97×10^6 mixed elements, which is not considered very fine off the body. The mesh points are packed near the solid surface, resulting in boundary layer mesh with a y^+ value of about 1 off the solid surface. An overall view of the isolated rotor mesh and a close-up view of the boundary layer mesh near the blade tip are shown in Fig. 2.

Computations were conducted with the arbitrary Mach number version of the U^{2}NCLE code using a parallel computer with 64 processors. For the steady-state solution, only one Newton subiteration was implemented at each time step. For unsteady time-accurate simulations, four Newton subiterations with eight symmetric Gauss–Seidel relaxations were normally used to converge the solution at each time step. Because of the Newton implicit scheme used to solve the nonlinear governing equations, a relatively larger minimum time step was adopted in the current computation, ranging from one to two azimuthal degrees per time step. This allows the user to choose the proper time step based on the flow physics instead of numerical stability. Both Spalart–Allmaras [19] and Wilcox's k–ω [20] turbulence models were used to model the viscous effect in the present investigation.

A. Validation with Test Data

The first case studied here is a steady-state flow validation. There are limited wind-tunnel test data for the Bell-Agusta 609 rotor available for comparison, except the 2-D pressure distribution at a section of 75% blade span. The freestream Mach number is 0.52, which approximates to the inflow speed of the 3-D rotor at 75% span location at the design rotor speed. To validate the code, two numerical computations were performed, one based on a 2-D mesh generated using the rotor cross-section profile at 75% of the span, and the second one based on the 3-D computational model to extract the data at 75% blade span. The collective pitch angle is 6.25 deg at 75% of the span, or 12 deg on the root for the 3-D rotor configuration.

Figure 3 shows the comparison of computed pressure coefficients along the airfoil section at 75% blade span for both 2-D and 3-D computational models. For comparison purpose the 2-D wind-tunnel test data were also superimposed in the plot. It is clear from the plot that the 2-D computational result correlates well with the experimental data. The leading edge suction peak is correctly predicted by the 2-D computational model. However, computed peak pressure extracted at 75% blade span from the 3-D computational model is underpredicted, because the flow condition is not exactly matched with the wind-tunnel test model. The computed leading edge suction peak is weaker compared to the 2-D model due to the three-dimensional effect.

B. Rotor in Hover Condition

The focus of the present study is to investigate the Bell-Agusta 609 rotor undergoing a higher harmonic blade-pitch oscillation, and its effect on the rotor flowfield, unsteady loads, and the tip vortex generated by the oscillating blades. To this end, simulations were first conducted for the hovering rotor with and without blade-pitch oscillation. The hover flow conditions are defined as follows: blade tip Mach number $M_{\text{tip}} = 0.69$, advance ratio $\mu = 0.0$, collective pitch angle $\theta_0 = 12$ deg at root, and coning angle $\beta_0 = 0$ deg. For the rotor with cyclic blade-pitch oscillation, the blade-pitch frequency is $f_r = 37.933$ Hz or 4 cycles per rotor revolution. The cyclic motion is defined as follows: $\beta_{1c} = \beta_{1s} = 0$ deg, $\theta_{1c} = 0$ deg, and $\theta_{1s} = 5$ deg. All three blades have the same phase angle ($\phi = 0$ deg) and the identical cyclic motion at any given time. Note that the cyclic motion specified in the current case causes excessive change in the blade-pitch angle (± 5 deg), which may not be applicable to the actual flight operation.

The unsteady simulation of the rotating blades started from zero wind speed, with the minimum time step of one azimuth degree and four Newton subiterations per time step. Simulations with five or more Newton subiterations per step were also tested, but found no significant improvement on the numerical accuracy and convergence of the unsteady solution. However, the computational time would increase considerably with the increase of Newton subiterations. The zero wind speed hover flow seemed to take a longer time to converge, with about 15 rotor revolutions to reach the periodic state.

For a rotor without cyclic pitching, the flowfield is steady at every azimuth location after the solution is fully converged. Figures 4 and 5 show predicted instantaneous swirl parameter and Mach number on the rotor tip-path plane (TPP) corresponding to three rotor instant locations, which covers one-quarter of blade revolution. The dominant feature of the hovering rotor flow is the tip vortex generated by the rotating blades, as shown by the swirl parameter in Fig. 4. The blade-vortex interaction is not apparent because the tip vortex is pushed down by the rotor wash flow, and therefore only part of the tip-vortex trajectory is seen on the tip-path plane. The tip-vortex trajectory is tracked for two-third revolution and then dissipated into the flowfield under the current grid resolution and the second-order accuracy of the algorithm. A refined computational mesh and/or using a higher-order numerical scheme may help tracking the tip vortex for a longer distance.

For the rotor with higher harmonic oscillation, all three blades have the identical cyclic pitching motion, which creates a repeated flow pattern corresponding to the blade oscillation frequency. Figures 6 and 7 show instantaneous swirl parameter and Mach number on the rotor tip-path plane corresponding to three blade positions: the maximum ($\alpha_1 = +5$ deg), the neutral ($\alpha_1 = 0$ deg), and the minimum ($\alpha_1 = -5$ deg) pitch angles. The swirl parameter in Fig. 6 highlights several interesting flow structures. Because the rotor blade undergoes a rather large variation in the effective pitching angle, a very different vortex structure is observed compared to the case without cyclic blade-pitch oscillation (Fig. 4). Vortex shedding and flow separation have been observed near the blade outboard at about 70–80% span location, as the rotor blade changed its pitch

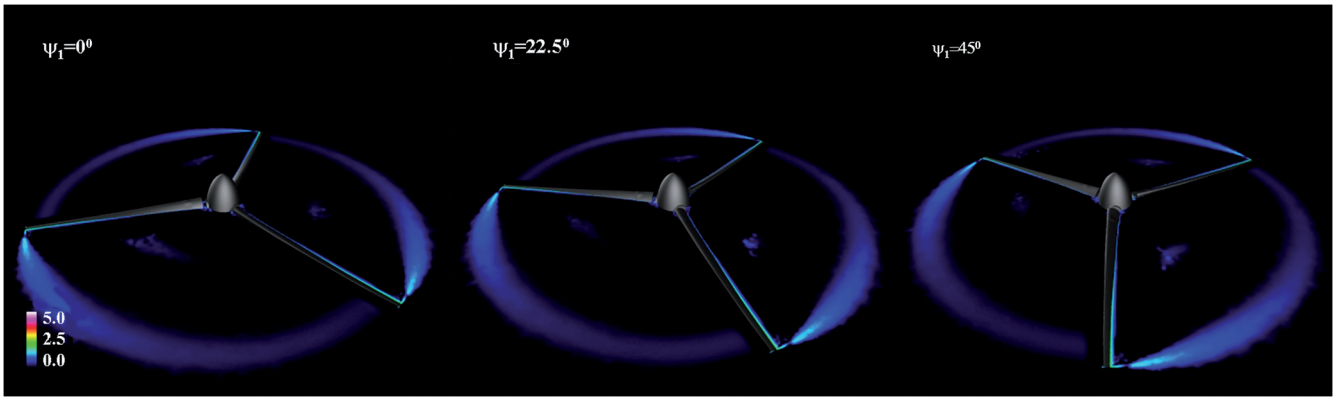

Fig. 4 Computed swirl parameter at three blade azimuth angles on the tip-path plane, HHC off.

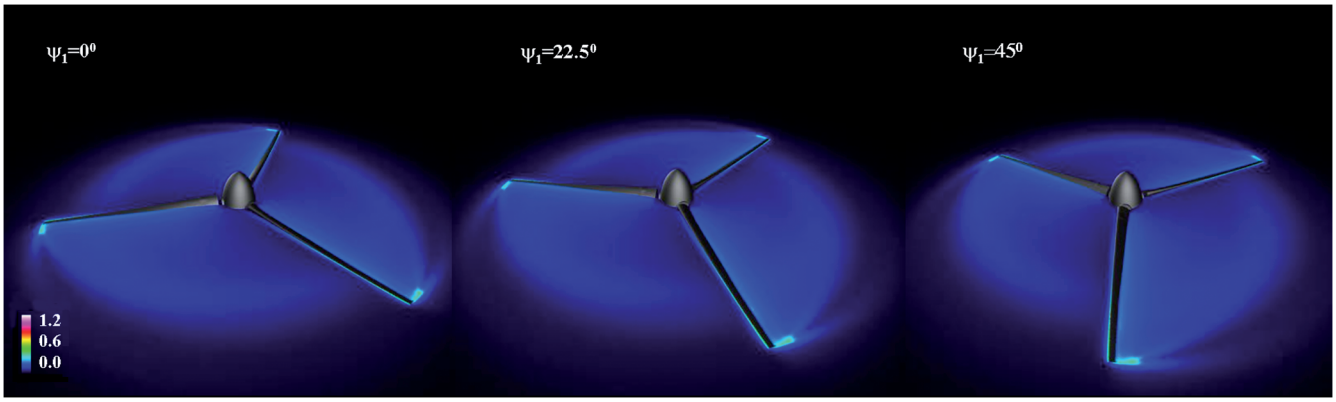

Fig. 5 Computed Mach number at three blade azimuth angles on the tip-path plane, HHC off.

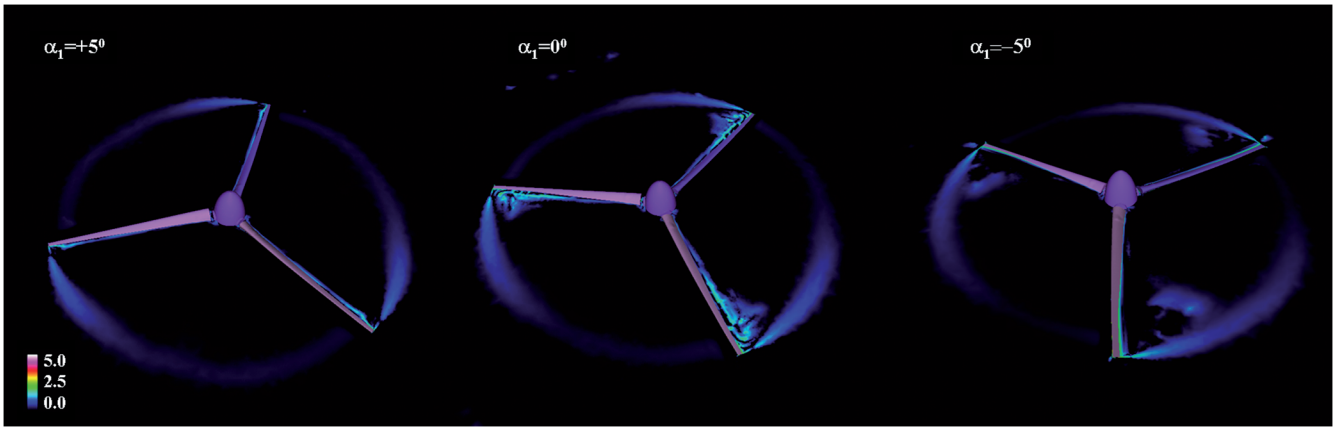

Fig. 6 Computed swirl parameter at three blade-pitch angles on the tip-path plane, HHC on.

angle from the uppermost to the downmost positions. A closer examination of the flowfield showed a pair of counter-rotating vortices (not shown here) formed on the upper blade surface during the downstroke cycle. The vortex shedding occurred when the oscillating blades almost reached the neutral position. However, no vortex shedding was observed when the blades reached the neutral position in the upstroke cycle. This is because the blade effective pitch angle is larger in the downstroke cycle than in the upstroke cycle. The unsteady solution also reveals the vortex–vortex interaction as the shedding vortex merged with the primary tip vortex (see Fig. 6). A localized high-speed region close to the speed of sound is found to accompany the vortex formation and shedding process, as clearly demonstrated in Fig. 7.

The higher-frequency cyclic blade pitch also causes pressure loading fluctuation on the blade surface due to excessive variation of the blade-pitch angle, resulting in unsteady loading over the azimuth. Figure 8 shows the behavior of the unsteady surface pressure distribution along the airfoil at the section of 75% blade span during the upstroke and downstroke cycles of the blade oscillation, where the arrows indicate the blade oscillation paths. It is seen that the pressure loading is increased as the blade-pitch angle increases (upstroke cycle), and is decreased as the blade-pitch angle decreases (downstroke cycle). Because of the periodic vortex shedding and flow separation near the outboard, there are pressure loading breaks at higher blade angles (Fig. 8), a similar phenomenon found in the light dynamic stall. This may not be desirable at the normal operating condition.

Figure 9 shows the variation of integrated lift, drag, and pitching moment coefficients over the blade pitching envelope. The unsteady airloads clearly follow the phase of the blade pitching angle and

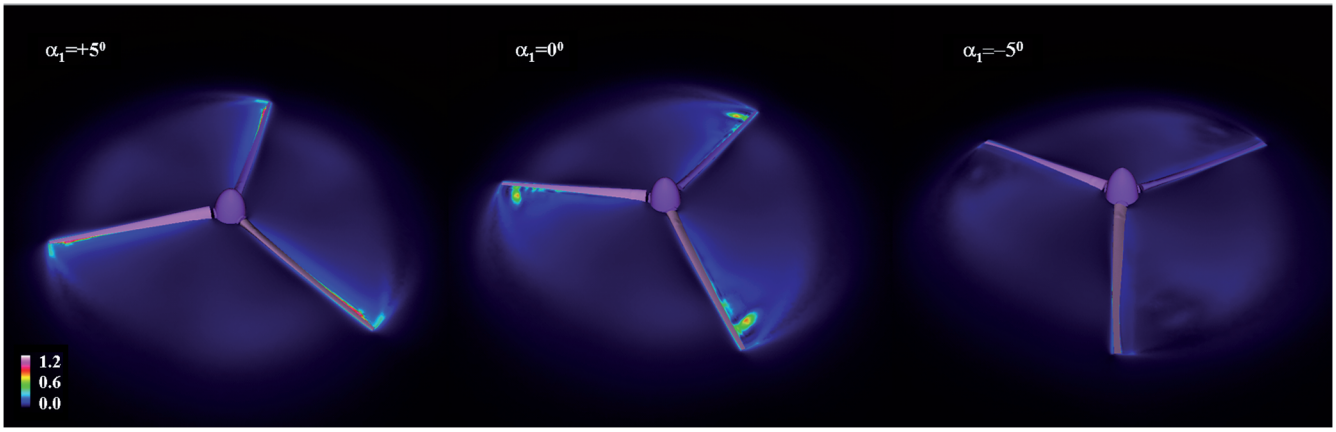

Fig. 7 Computed Mach number at three blade-pitch angles on the tip-path plane, HHC on.

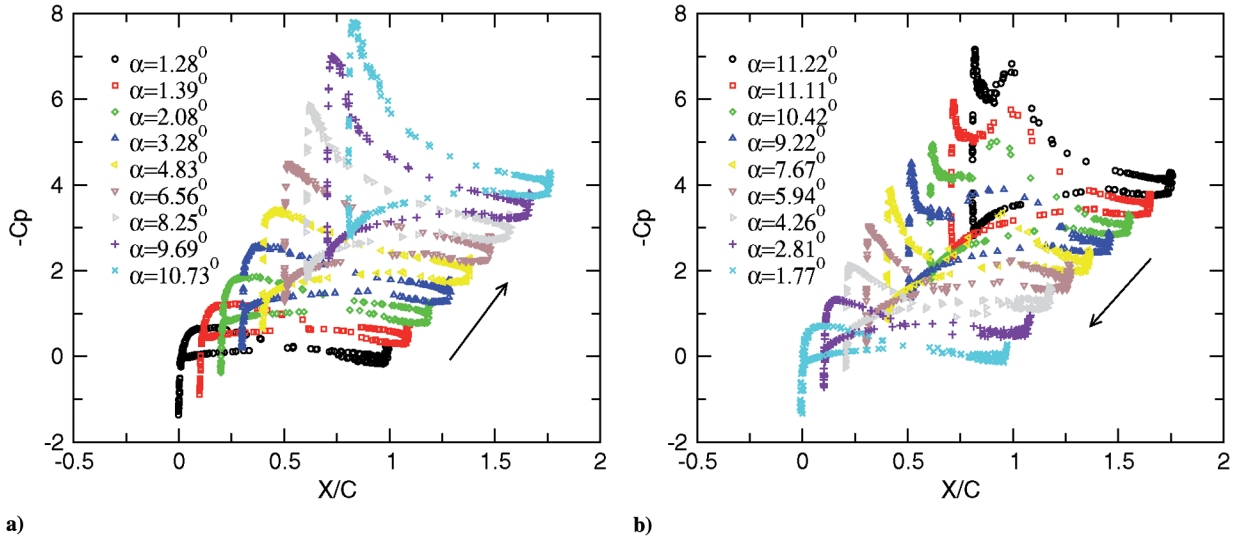

Fig. 8 Computed unsteady pressure distributions at 75% blade span in a) upstroke and b) downstroke cycles.

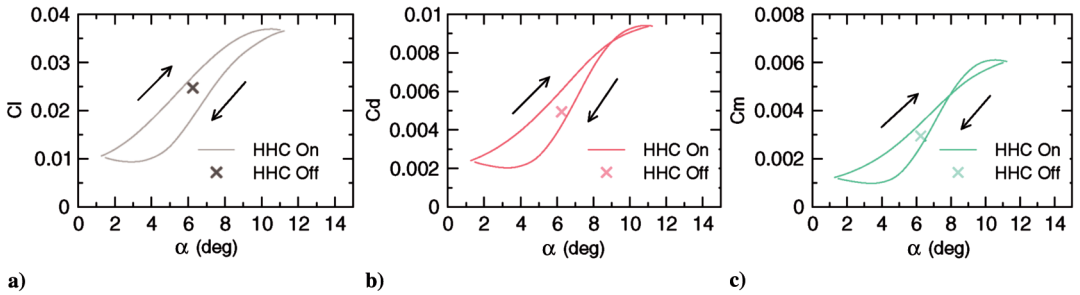

Fig. 9 Integrated a) lift, b) drag, and c) pitching moment coefficients with blade-pitch oscillation.

frequency. The integrated airloads do not show noticeable breaks over the entire pitching angle as observed in the pressure loading at 75% span location, because the vortex shedding and flow separation are localized near the outboard region, which only contributes to a portion of the integrated forces.

C. Rotor in Forward-Descent Flight

In the previous investigation, the tip vortex generated by the hovering rotor was pushed downward, and the blade-vortex interaction was not immediate. One of the potential benefits of the higher harmonic blade-pitch oscillation is to reduce the blade-vortex interaction noise, as reported on the XV-15 rotor model test at NASA Ames Research Center [3]. To investigate the blade-vortex interaction phenomenon for the Bell-Agusta 609 rotor undergoing a higher harmonic blade-pitch oscillation, a low-speed forward flight is considered where the blade-vortex interaction is most significant. Simulations were performed with the following rotor conditions: tip Mach number $M_{\text{tip}} = 0.69$, advance ratio $\mu = 0.15$, descent angle $\delta = 8$ deg, collective pitch angle $\theta_0 = 12$ deg at root, and coning angle $\beta_0 = 0$ deg. For a rotor with the cyclic pitch oscillation, the blade-pitch frequency is $f_r = 37.933$ Hz or 4 cycles per rotor revolution. The cyclic motion is specified as $\beta_{1c} = \beta_{1s} = 0$ deg, $\theta_{1c} = 0$ deg, and $\theta_{1s} = 5$ deg. All three blades have the same cyclic motion as in the previous case, except that the current simulation involves a freestream velocity.

Simulations of the Bell-Agusta 609 rotor in forward-descent flight were performed with the same numerical options as used in the hovering rotor. However, unlike the previous case, the unsteady

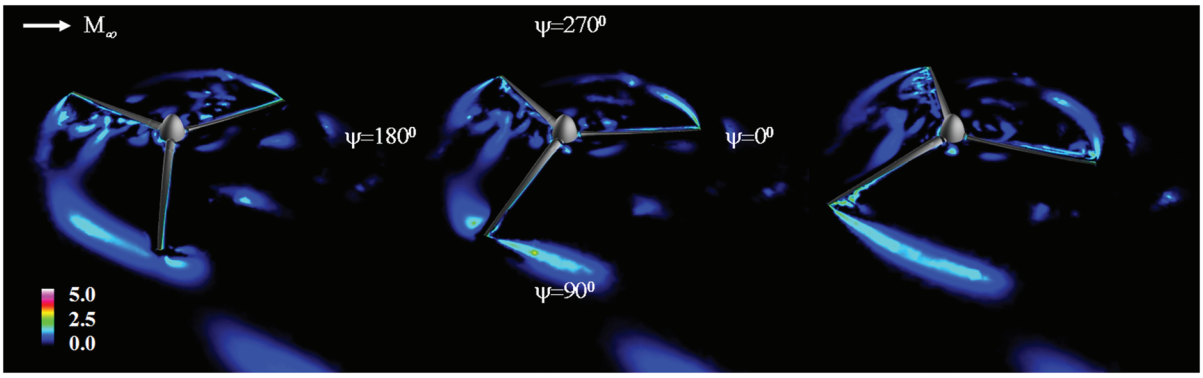

Fig. 10 Computed swirl parameter on tip path plane with blade-pitch oscillation.

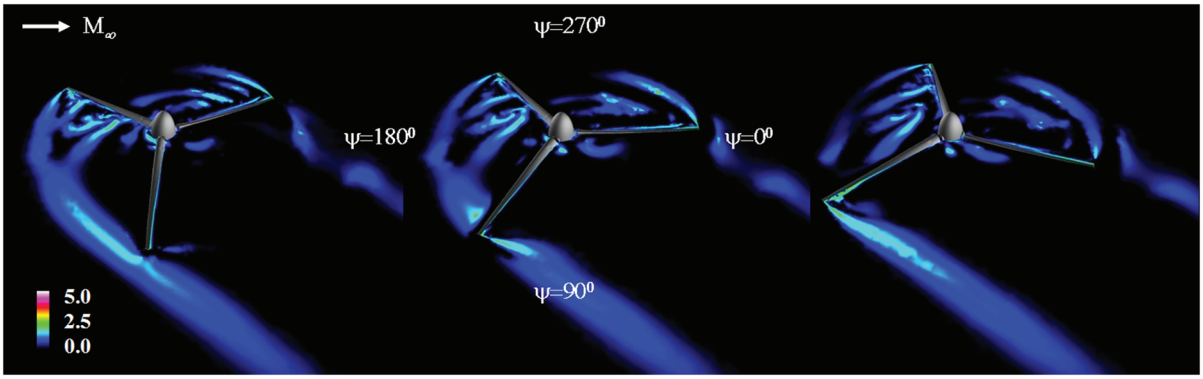

Fig. 11 Computed swirl parameter on tip path plane without blade-pitch oscillation.

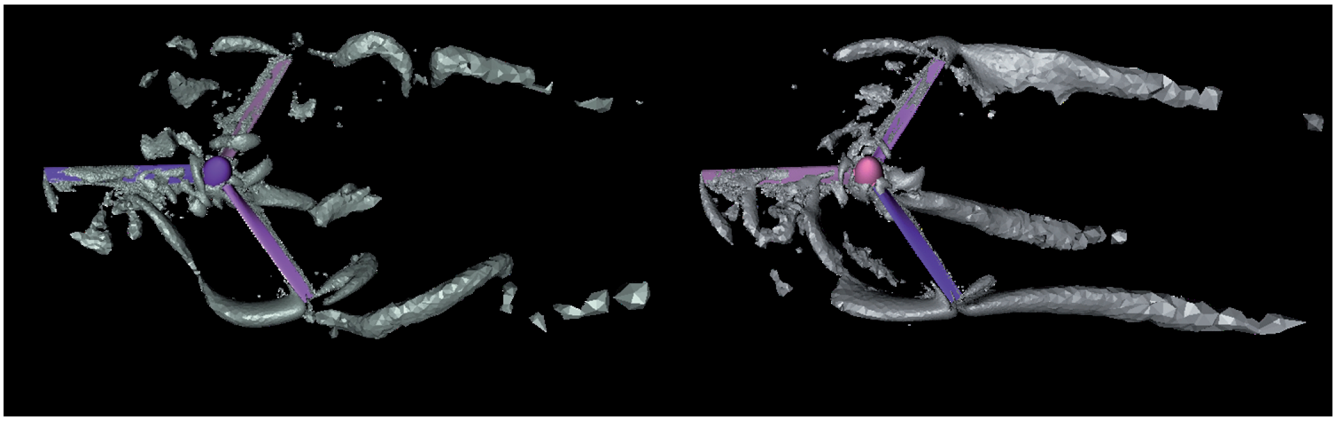

Fig. 12 Comparison of tip-vortex trajectories by isoswirl parameters with HHC on and off.

solutions were converged rather quickly to the periodic state in about 5 rotor revolutions for the forward-descent flight condition.

Figures 10 and 11 compare the wake structures visualized by the swirl parameter for a rotor with and without higher harmonic blade-pitch oscillation. The most dominating feature of the flowfield is the blade-vortex interaction, which is evident for the advancing and retreating blades in the second and third quadrants. Wake structures also show multiple blade-vortex and vortex–vortex interactions, although many of them are smeared quickly due to the numerical dissipation. As demonstrated by the isoswirl parameter in Fig. 12, the most significant distinction of the two wake structures is the trajectory of the tip vortex. The path of the tip vortex generated by the advancing blade is significantly curved due to the blade oscillation, whereas the path of the tip vortex without blade oscillation is relatively straight.

Figures 13 and 14 compare computed normal forces and pitching moments on the rotor disk with and without the blade-pitch oscillation, where the rotor rotates in the clockwise direction. The most apparent difference in the plots is the overall flow patterns. Although the extremes of the normal forces and pitching moments with and without blade-pitch oscillation both occur near the outboard in the second quadrant, there is a phase delay of about 22 deg due to the blade-pitch oscillation. Secondly, there are four peaks for the normal force and pitching moment in the oscillating blade case compared to only one peak in the nonoscillating blade case. In both solutions, there are significant blade-vortex interactions which dominant the airloads.

To further investigate the blade-vortex interaction phenomena with and without higher harmonic blade-pitch oscillation, unsteady sectional normal force and pitching moment at three blade spans, $r/R = 0.68$, 0.81, and 0.94, are plotted over the whole azimuth. The sectional normal forces are compared in Figs. 15 and 16, and sectional pitching moments are compared in Figs. 17 and 18, respectively. In both cases, the blade-vortex interaction normal force and pitching

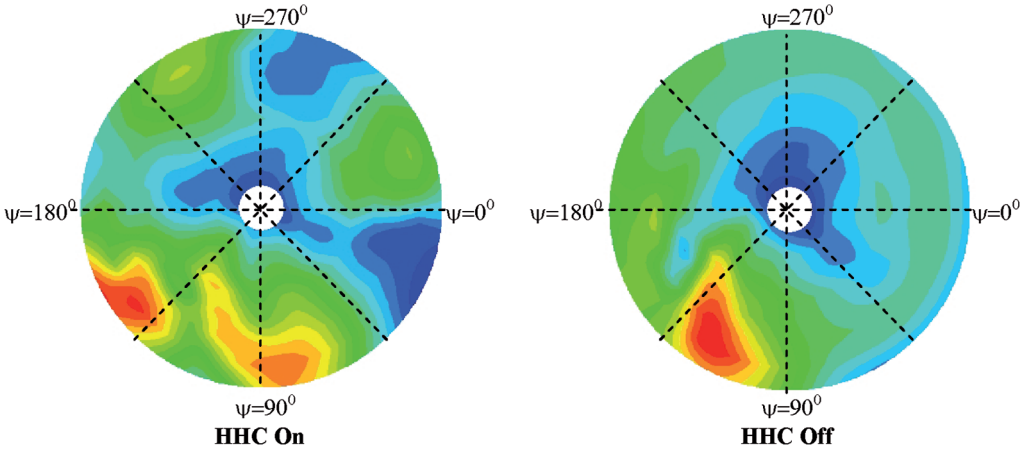

Fig. 13 Predicted rotor disk normal force coefficients around azimuth.

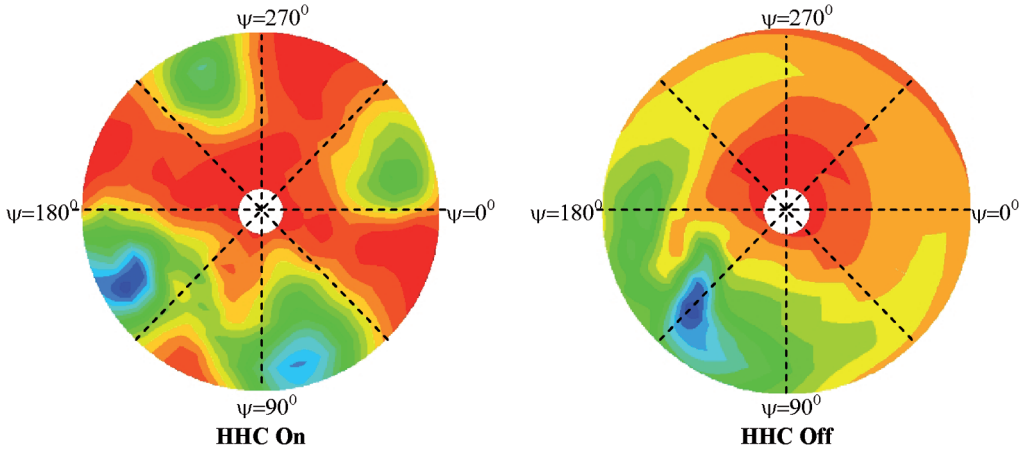

Fig. 14 Predicted rotor disk pitching moment coefficients around azimuth.

moment impulses are well demonstrated in the computations. For the nonoscillating blade case, all three blades interact with the tip vortex at the same azimuth location (about 130–160 deg). For the oscillating blade case, however, the location of the blade-vortex interaction for each blade varies in azimuth because of the unsteadiness of the tip-vortex trajectory. Careful studies of the sectional normal force and pitching moment at $r/R = 0.64$ and 0.81 (Figs. 15 and 17) indicate that each blade interacts with the tip vortex quite differently in the second quadrant. Although there is only one primary blade-vortex interaction impulse found from 120 to 140 deg azimuth for blade 1 and blade 2, two blade-vortex interaction impulses are seen for blade 3, one from 75 to 100 deg and another one from 120 to 130 deg. This indicates that the curved tip vortex generated by the oscillating blade (Fig. 12) was cut through twice by blade 3 at the above two locations. In general, higher harmonic blade-pitch oscillation causes excessive airload vibration around whole azimuth, equivalent to what is caused by the blade-vortex interaction. However, for the oscillating blade case, the blade that interacts twice with the tip vortex seems to have weak blade-vortex interaction impulses than the other two blades, as demonstrated in Figs. 15 and 17.

As indicated by Yu et al. [21], the blade-vortex interaction is one of the major sources of the noise, unsteady loads, and vibration for the helicopter rotors. The strength of the blade-vortex interaction can be affected by many factors, such as miss distance, vortex core size, vortex trajectory, and vortex strength. Certainly some of these factors have been changed by the blade-pitch oscillation, as have been demonstrated in the present study. Nevertheless, applying this concept to the actual rotor design requires further studies to balance the benefit and penalty it may bring, and also to discover the optimal design parameters in order to achieve the desired objective.

IV. Conclusions

The unsteady simulations for the Bell-Agusta 609 rotor in hover and forward-descent flight were performed using an unstructured flow solver U^{2}NCLE. An embedded dynamic moving grid capability was presented and demonstrated to model the rotor blades undergoing a higher harmonic blade-pitch oscillation. The effects of the blade-pitch oscillation were investigated on the unsteady airloads, tip-vortex structures, and associated blade-vortex interaction in hover and low-speed forward-descent flight. The results and flow phenomena revealed in the numerical simulations may be useful to the increased understanding of the blade-pitch oscillation for the noise, airloads, vibration alleviation, and to the future development of these concepts to improve aerodynamic and acoustic design of helicopter rotors. The following concluding remarks are given for the current study:

1) The embedded dynamic moving grid technique presented in this work is very flexible, robust, and efficient to handle single or multiple rotors with complex rigid blade cyclic motions. A unique advantage of the current method is that no interpolation is required to exchange the information between the relative moving grids. This preserves the same numerical accuracy at the interface as that in the interior domain, which is very useful for the development of higher-order numerical schemes.

2) The rotor in hover with blade-pitch oscillation generates periodic vortex shedding and flow separation near the outboard under the current cyclic pitch scheme. The vortex shedding occurs at the outboard blade during the downstroke cycle of the blade-pitch oscillation, which causes pressure loading breaks at the same span location. However, the integrated forces and pitching moment are not affected because the pressure loading break occurs only in a localized region for a short period of time.

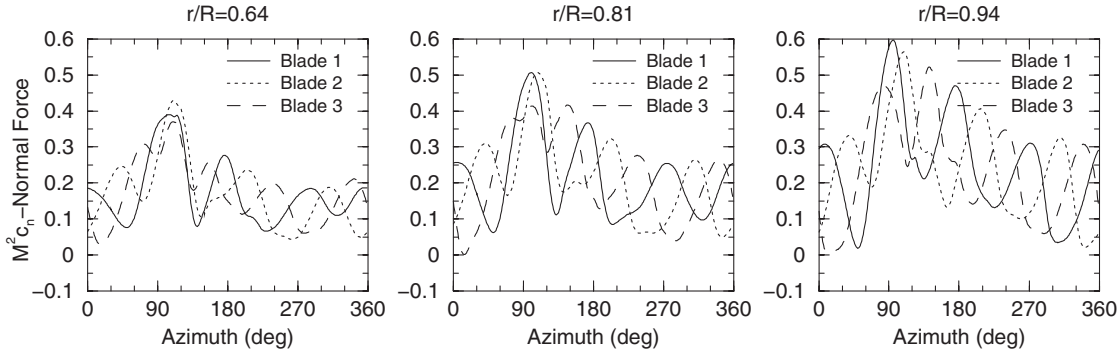

Fig. 15 Unsteady sectional normal force coefficients with HHC.

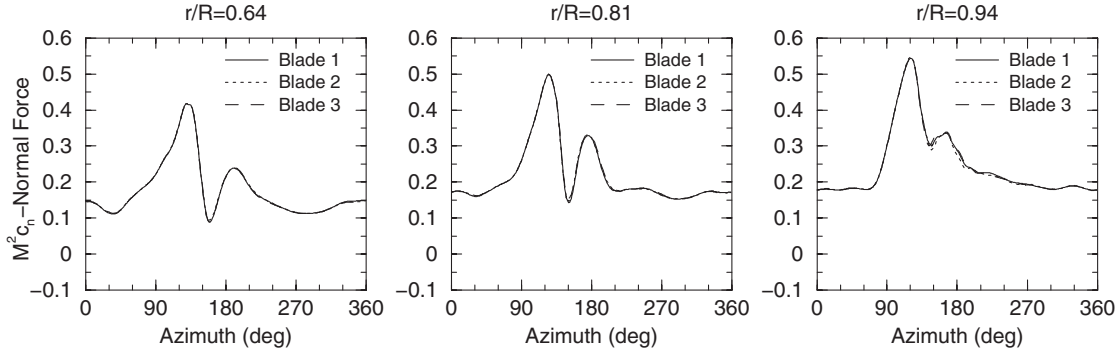

Fig. 16 Unsteady sectional normal force coefficients without HHC.

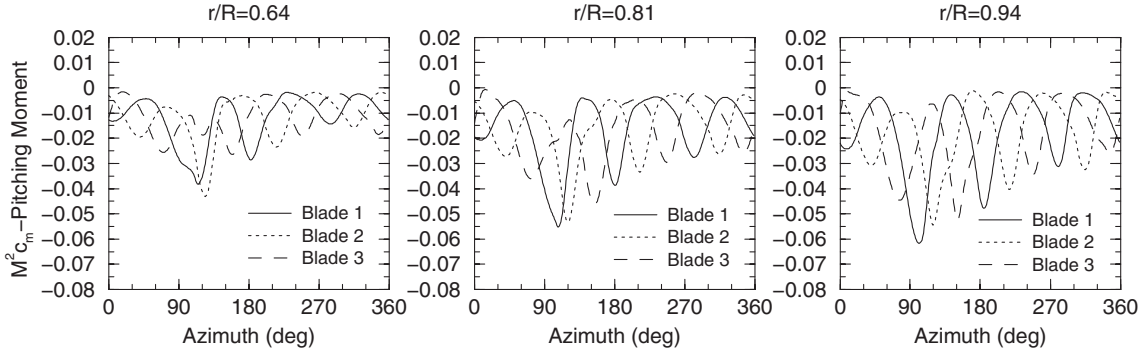

Fig. 17 Unsteady sectional pitching moment coefficients with HHC.

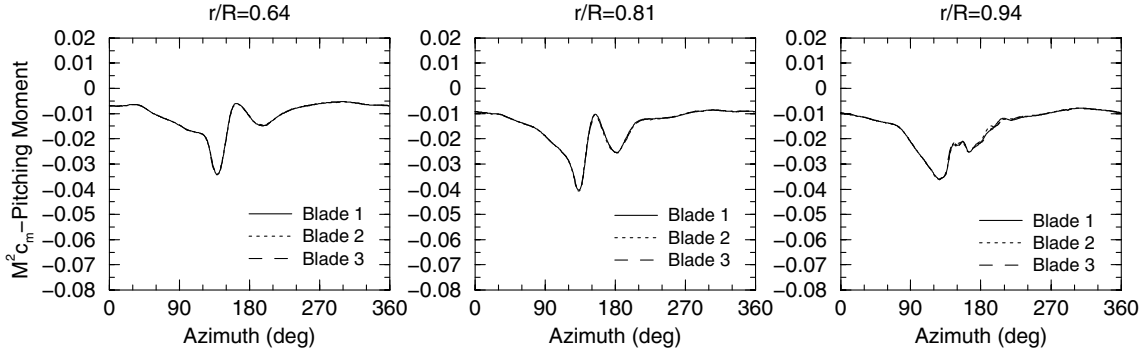

Fig. 18 Unsteady sectional pitching moment coefficients without HHC.

3) For the rotor in low-speed forward-decent flight, the blade-pitch oscillation significantly alters the trajectory of the tip vortex generated by the advancing blade and thus the way the blades interact with the tip vortex. The blade-vortex interaction normal force and pitching moment impulses are well demonstrated in the simulations. However, excessive vibratory airloads are experienced in the whole azimuth due to the blade-pitch oscillation.

4) To improve the rotor aerodynamic performance and alleviate the noise and vibratory loads, the higher harmonic blade-pitch control parameters must be optimized through extensive numerical and/or experimental tests, based on the underlying mechanism for the rotor noise and vibration in various flight conditions.

Acknowledgments

The authors are grateful to Bell Helicopter Textron, Inc., for providing the geometry of the Bell-Agusta 609 rotor and granting the permission to publish the results. Thanks also go to Xiao Wang of the Computational Simulation and Design Center at Mississippi State University for generating the images and plots in this work.

References

[1] Brooks, T. F., Booth, E. R., Boyd, D. D., Splettstinesser, W. R., Schultz, K. J., Roland, N., Georg, H., and Stregy, O., "HHC Study in the DNW to Reduce BVI Noise-An Analysis," *International Technical Specialists Meeting on Rotor Acoustics and Rotor Fluid Dynamics*, American Helicopter Society/RAeS, Alexandria, VA, 15–17 Oct. 1991.

[2] Yu, Y. H., Gmelin, Y. B., Heller, H., Philippe, J. J., Mercker, E., and Preisser, J. S., "Higher Harmonic Control Aeroacoustics Test—The Joint German/French/US HART Project," *20th European Rotorcraft Forum*, Netherlands Association of Aeronautical Engineers, Amsterdam, The Netherlands, 4–7 Oct. 1994.

[3] Nguyen, K., Betzina, M., and Kitaplioglu C., "Full-Scale Demonstration of Higher Harmonic Control for Noise and Vibration Reduction on the XV-15 Rotor," *American Helicopter Society 56th Annual Forum*, American Helicopter Society, Alexandria, VA, 2–4 May 2000.

[4] Caradonna, F., and Tung, C., "Experimental and Analytical Studies of a Model Helicopter Rotor in Hover," NASA TM-82323, Sept. 1981.

[5] Duque, E., Biswas, R., and Strawn, R., "A Solution-Adaptive Structured/Unstructured Overset Grid Flow Solver with Applications to Helicopter Rotor Flows," AIAA Paper 95-1766, June 1995.

[6] Amhad, J. U., and Strawn, R. C., "Hovering Rotor and Wake Calculations with an Overset-Grid Navier-Stokes Solver," *American Helicopter Society International 55th Annual Forum Proceedings*, American Helicopter Society, Alexandria, VA, May 1999, Vol. 2, pp. 1949–1959.

[7] Potsdam, M., Yeo, H., and Johnson, W., "Rotor Airloads Prediction Using Loose Aerodynamic/Structural Coupling," *American Helicopter Society 60th Annual Forum*, American Helicopter Society, Alexandria, VA, June 2004.

[8] Duque, E. P. N., Sankar, L., Menon, S., Bauchau, O., Ruffin, S., Smith, M., Ahuja, K., Brentner, K., Long, L., Morris, P., and Gandhi, F., "Revolutionary Physics-Based Design Tools for Quiet Helicopters," AIAA Paper 2006-0994, Jan. 2006.

[9] Chan, W. M., Meakin, R. L., and Potsdam, M. A., "CHSSI Software for Geometrically Complex Unsteady Aerodynamic Applications," AIAA Paper 2001-0593, Jan. 2001.

[10] Strawn, R., and Barth, T., "A Finite-Volume Euler Solver for Computing Rotor-Wing Aerodynamics on Unstructured Meshes," *Proceedings of 48th Annual Forum of American Helicopter Society*, American Helicopter Society, Alexandria, VA, 3–5 June 1992.

[11] Hyams, D. G., Sreenivas, K., Sheng, C., Briley, W. R., Marcum, D. L., and Whitfield, D. L., "An Investigation of Parallel Implicit Solution Algorithms for Incompressible Flows on Multi-Element Unstructured Topologies," AIAA Paper 2000-0271, Jan. 2000.

[12] Sheng, C., and Wang, X., "Characteristic Variable Boundary Conditions for Arbitrary Mach Number Algorithm in Rotating Frame," AIAA Paper 2003-3076, 23–26 June 2003.

[13] Briley, W. R., McDonnald, H., and Shamroth, S. J., "A Low Mach Number Euler Formulation and Application to Time-Iterative LBI Schemes," *AIAA Journal*, Vol. 21, No. 10, Oct. 1983, pp. 1467–1469.

[14] Briley, W. R., Tayler, L. K., and Whitfield, D. L., "High-Resolution Viscous Flow Simulations at Arbitrary Mach Number," *Journal of Computational Physics*, Vol. 184, No. 1, 2003, pp. 79–105. doi:10.1016/S0021-9991(02)00018-9

[15] Sheng, C., and Wang, X., "A Global Preconditioning Method for Low Mach Number Viscous Flows in Rotating Machinery," American Society of Mechanical Engineers Paper GT2006-01189, 8–11 May 2006.

[16] Leishman, J. G., *Principles of Helicopter Aerodynamics*, 2nd ed., Cambridge Univ. Press, Cambridge, England, U.K., 2006.

[17] Narramore, J., Lancaster, G., and Sheng, C., "Application of Computational Fluid Dynamics During the Conceptual Design of the Bell JHL QUAD-Tiltrotor," *American Helicopter Society Forum 63*, American Helicopter Society, Alexandria, VA, 1–3 May 2007.

[18] Marcum, D. L., and Gaither, J. A., "Mixed Element Type Unstructured Grid Generation for Viscous Flow," AIAA Paper 99-325A, 28 June–1 July 1999.

[19] Spalart, P., and Allmaras, S., "A One-Equation Turbulence Model for Aerodynamic Flows," AIAA Paper 92-0439, Jan. 1992.

[20] Wilcox, D. C., *Turbulence Modeling for CFD*, DCW Industries, La Canada, CA, 1998.

[21] Yu, Y. H., Tung, C., Gallman, J., Schultz, K. J., Wall, B., van der, Spiege, P., and Michea, B., "Aerodynamics and Acoustics of Rotor Blade-Vortex Interactions," *Journal of Aircraft*, Vol. 32, No. 5, Sept.–Oct. 1995, pp. 970–977.